Combining radial point interpolation meshless method with a new homogenization technique for trabecular bone multiscale structural analyses

Marco Marques[1, 5]*, Jorge Belinha[1, 2], António F. Oliveira[3],
M.C. Manzanares-Céspedes[4], Renato Natal Jorge[1, 5]

[1] INEGI – Institute of Science and Innovation in Mechanical and Industrial Engineering, Porto, Portugal.
[2] ISEP – Department of Mechanical Engineering, School of Engineering, Polytechnic of Porto, Porto, Portugal.
[3] ICBAS – Institute of Biomedical Sciences Abel Salazar, University of Porto, Porto, Portugal.
[4] Muscular and Skeletal Pathology Research, Human Anatomy and Embryology Unit, Universitat de Barcelona, Barcelona, Spain.
[5] FEUP – Department of Mechanical Engineering, Faculty of Engineering, University of Porto, Porto, Portugal.

Purpose: Bone tissue is a dynamic tissue, possessing different functional requirements at different scales. This layered organization indicates the existence of a hierarchical structure, which can be characterized to distinguish macro-scale from micro-scale levels. Structurally, both scales can be linked by the use of classic multiscale homogenization techniques. Since in bone tissue each micro-scale domain is distinct form its neighbour, applying a classic multiscale homogenization technique to a complete bone structure could represent an inadmissible computational cost. Thus, this work proposes a homogenization methodology that is computationally efficient, presenting a reduced computational cost, and is capable to define the homogenized microscale mechanical properties of the trabecular bone highly heterogeneous medium. *Methods:* The methodology uses the fabric tensor concept in order to define the material principal directions. Then, using an anisotropic phenomenological law for bone tissue correlating the local apparent density with directional elasticity moduli, the anisotropic homogenized material properties of the micro-scale patch are fully defined. To validate the developed methodology, several numerical tests were performed, measuring the sensitivity of the technique to changes in the micro-patch size and preferential orientation. *Results:* The results show that the developed technique is robust and capable to provide a consistent material homogenization. Additionally, the technique was combined with two discrete numerical techniques: the finite element method and radial point interpolation meshless method. *Conclusions:* Structural analyses were performed using real trabecular patches, showing that the proposed methodology is capable to accurately predict the micro-scale patch mechanical behavior in a fraction of the time required by classic homogenization techniques.

Key words: meshless methods, radial point interpolation method, fabric tensor, homogenization technique, multiscale

1. Introduction

Bone is a mineralized biological structure defined by bone matrix and bone cells. Among many other functions, bone is designed to structurally support soft tissues in the body. The renew of bone occurs by a biological process called bone remodeling [20]. In addition to its morphology adaptation, bone also changes its macro-scale mechanical properties to fulfill and optimize the specific physiological function of structural support [6]. In order to understand bone structure and biological and mechanical functions bone can be classified in different hierarchical structures, constituted of many scale levels with specific interactions and with very complex architectures [10]. Some authors classify bone with different structural levels from the macroscale (whole bone) to sub-nano-

---

scale (hydroxyapatite crystals, constituent of the inorganic phase of bone and TC molecules) [1]. Since the bone has different functional requirements at different scales, to analyze the equivalent (homogenized) mechanical behavior of bone material, it is necessary to investigate the mechanical properties of its distinct components and the structural relationships between such components at different scales [13]. Many researchers have addressed the study of bone mechanical behavior by developing analytical and numerical models. Thus, to describe the mechanical behavior of bone at certain scale levels, some models apply multiscale approaches and other use homogenization techniques combined with distinct discretization approaches, such as finite element methods (FEM). Today, it is generally accepted that bone remodeling is mainly caused by the transient nature of its strain/stress fields (induced by the external loads applied in its physical boundary). This simple concept was first proposed by Wolff in 1886 [21]. Wolff reported that the directions of the external applied loads directly influences the direction of the trabecular bone, since bone cell sense the applied loads and change their physical disposition and distribution (modifying the local and global bone morphology).

The study of bone remodeling using numerical approaches evolved significantly since the first simplistic models, which considered bone as an isotropic-elastic material only sensitive to mechanical stimuli [5], [11]. Year after year, the complexity of bone models started to increase. Some authors started to consider the trabecular orientation (material anisotropy), and others developed bio-mechanical models assuming both mechanical and biological stimuli. More recently, multiscale models were successfully developed.

Trabecular bone is the major responsible for the bone metabolic activity, in which is included the remodeling process. The typically trabecular bone architecture leads to a highly heterogeneous medium, showing anisotropic material properties. Thus, some authors started to characterize bone mechanical properties, considering and encoding the orientation and anisotropy of the material [16]. These authors used the fabric tensor concept **A**, a symmetric second rank tensor that characterizes the arrangement of a multiphase material. Back in 1985, Cowin [7] described the relation between the fabric tensor and the fourth rank elasticity tensor $\mathbf{C}_{ijkl}$. Cowin also showed that the fabric tensor provides an ellipsoid that can be associated with the varieties of material symmetries observed in many natural materials. Presently, two different techniques are available to estimate the fabric tensor, the mechanical-based techniques and the morphologic-based techniques (morphologic-based use the interface between phases of the material to estimate the fabric tensor). Thus, naturally, morphologic-based techniques are commonly used to define the fabric tensor of bone tissue. Most of the available techniques, using morphologic-based methods, obtain the fabric tensor applying an orientation distribution function (ODF), which is estimated from an orientation-dependent feature of interest. In the literature it is shown that when the ODF data is disposed on a polar plot and fitted in an ellipse, the corresponding ellipse parameters can be correlated with the material orientation/anisotropy. [8], [15], [19], [22]. Material mechanical properties can be estimated experimentally (using mechanical tests) or virtually (using concepts as the fabric tensor). Such estimation is of high importance since it feeds constitutive laws. Then, combining the constitutive laws with discrete numerical methods, it is possible to predict the material structural behavior. Thus, an accurate and robust model depends on three blocks: an accurate predictor of the material properties, a reliable constitutive law and an accurate discrete numerical method.

Discrete numerical techniques enables the researchers to discretize the problem domain in small parts (elements in the FEM and nodes in meshless methods). Then, a variational principle (governing the physical phenomenon) is applied to obtain an algebraic system of equations. Solving such equation system permits to access the variable field of interest (such as the displacement or the strain/stress fields). The first discrete numerical technique applied to orthopedic biomechanics, in 1972, was the FEM and it was used to evaluate stresses in human bones [12]. In order to answer to some discretization drawbacks of FEM, other discretization techniques, such as meshless methods, have been developed. In the literature it is possible to find several distinct meshless methods techniques [2], [4], [14], [18].

The main objective of this work is to combine a new developed homogenization technique, in which the fabric tensor concept in synergy with a previous developed bone tissue material law is applied, with the Radial Point Interpolation Method (RPIM) meshless method, aiming to achieve a low-cost and efficient multiscale technique.

2. Materials and methods

In this section the RPIM formulation is briefly presented. Also, the nodal connectivity, integration mesh, shape functions and elasto-static linear equations used in

this formulation are explained. The proposed homogenization technique is also fully presented.

2.1. Radial Point Interpolation method formulation

Meshless methods, unlike the FEM, do not use elements or any other lattice discretization to establish nodal/particle connectivity. With meshless methods, the problem domain is discretized using an unstructured nodal set where nodes can be distributed regularly or irregularly. These methods have advantages in the field of biomechanics, since they are capable of discretize highly complex problem domains using information gathered directly from medical images [2]. In meshless methods, the nodal discretization only requires the spatial coordinates of the nodes and, possibly, its individual material properties. The nodal connectivity (how each node interacts with its neighbor) is obtained using geometrical and mathematical constructions, allowing the researchers to define the influence-domain concept, the equivalent to the element concept in the FEM. In this work, meshless methods are combined with weak formulations to solve in integro-differential equations. Thus, the construction of a background integration mesh, which can be nodal-dependent or nodal-independent, is mandatory, to enable the numerical integration of such equations. Only the meshless methods that use nodal dependent constructions are called truly meshless methods, because they enable us to directly define the spatial position and the integration weight of all integration points using only the spatial positions of the nodes [2]. Concerning the construction of shape functions, RPIM shape functions are obtained using the Radial Point Interpolators (RPI) technique. In this technique, a radial basis function is combined with a polynomial basis function [18]. Despite the classical RPI formulation uses polynomial basis functions, previous works have shown that they are unnecessary if RBF's shape parameters are chosen carefully [2]. This is an important innovation since it allows to increase its computational efficiency. Nonetheless, in this work, it is assumed the classical RPI formulation. Therefore, considering the function $h(x_I)$ defined in the domain $\Omega \subset \mathbb{R}^2$ the value of function $h(x_I)$ at the point of interest x_1 is defined by Eq. (1),

$$h(x_I) = \sum_{i=1}^{n} R_i(x_I)a_i(x_I) + \sum_{j=1}^{m} P_j(x_I)b_j(x_I)$$

$$= R(x_I)^T a(x_I) + P(x_I)^T b(x_I) \qquad (1)$$

where $R_i(x_I)$ is the RBF, n is the number of nodes in the influence-domain of x_I. The coefficients $a_i(x_I)$ and $b_j(x_I)$ are the non-constant coefficients of $R_i(x_I)$ and $p_j(x_I)$, respectively. The monomials of the polynomial basis are defined by $p_j(x_I)$ and m is the basis monomial number. The variable r_{ij} is the distance between the relevant node $xi = \{x_i, y_i\}^T$ and the neighbor node $x_j = \{x_j, y_j\}^T$, $r_{ij} = \sqrt{(x_j - x_i)^2 + (y_j - y_i)^2}$. Several known RBFs are well studied and developed in [2]. This work uses the Multiquadric (MQ) function $R(r_{ij}) = (r_{ij}^2 + c^2)^p$, where c and p are two parameters that need to be optimized, since they affect the performance of the RBFs. Notice that each integration weight should possesses its own c parameter. Thus, for integration point I with an integration weight $\hat{\omega}_I$, the shape parameter c is obtained with: $c_I \cong \gamma \hat{\omega}_I$. This spatial dependence of the RBF's shape parameter is demonstrated in research works available in the literature [2]. Previous works on the RPIM found that parameter γ should be close to zero, $\gamma \cong 0$, and p should be close to one, $p \cong 1$ [2]. However, these values cannot be $\gamma = 0$ and $p = 1$. The use of the exact integer value for p leads to a singular moment matrix and assuming a null γ leads to singular moment matrix. Furthermore, previous works [2] have shown that values of p very close to the unit enable us to obtain the most accurate solutions (regardless the analyzed problem). Thus, the authors have decided to use $p = 1.0001$ or $p = 0.9999$. Additionally, as shown in [2], the parameter γ should be very close to zero, because as its value grows, the RPI shape function loses its interpolation properties. Thus, the authors have selected $\gamma = 0.0001$ in order to "maximize" the RPI interpolation properties. Commonly, the polynomial basis has to possess a low degree to guarantee that the interpolation matrix of RBF is invertible. Thus, in this work the constant polynomial basis is used: $p^T(x) = \{1\}$; $m = 1$. The polynomial basis has to satisfy an extra requirement in order to obtain an unique solution [2]

$$\sum_{i=1}^{n} p_j(x_i)a_j(x_i) = 0, \quad j = 1, 2, ..., m, \qquad (2)$$

in which n represents the number of nodes inside the influence-domain of interest point x_I. Comparing RPIM with other meshless methods, it has lower computational cost during the processing phase of the numerical analysis (after the construction of the nodal connectivity, integration mesh and shape functions) and shows a higher re-meshing flexibility and a higher accuracy on the solution variable field [9].

2.2. Homogenization technique

The homogenization technique used in this word is fully described in this section. In this work, a micro-CT from the cuboid bone was used. First, since this work is 2D, only a CT-slice was considered. Then, for the selected thin slice of bone tissue, a square Region of Interest (ROI) was identified. Afterwards, the fabric tensor concept was applied to that ROI, allowing to determine the material preferential orientation. In addition, using a bone tissue phenomenological law, the pixel information of the selected ROI was used to obtain the homogenized material properties of the microscale patch. This homogenization technique enabled us to define the homogenized anisotropic material proprieties of the trabecular bone, a highly heterogeneous material. The algorithm describing the proposed homogenization technique is presented in Fig. 1 and its features are presented in the following subsections.
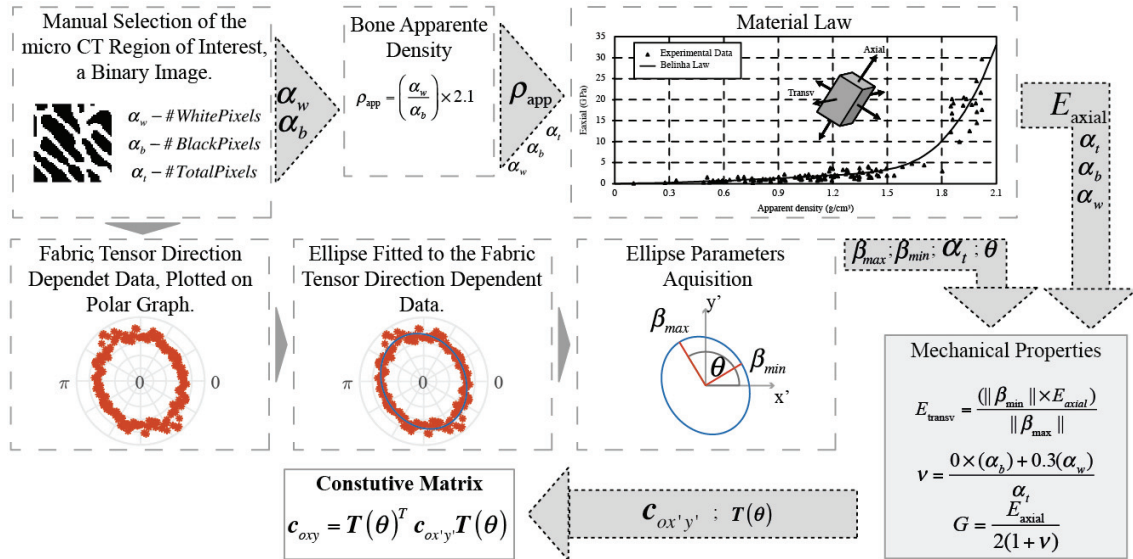
direction τ, with the interface between both phases of the material is counted, $Int(\tau)$. Furthermore, the length of the parallel lines family, h for the τ direction was also obtained. Possessing h and τ, it was possible to define the orientation distribution function (ODF), which in this case is called mean interception length (MIL), Eq. (3).

$$MIL(\tau) = \frac{h}{Int(\tau)}. \qquad (3)$$

In the literature, it is possible to find several works showing the robustness and accuracy of this technique in the prediction of the material properties of trabecular bone [8], [19], [22]. The work of Moreno et al. [15] shows that when the ODF data is disposed on a polar plot and fitted in an ellipse, the corresponding ellipse parameters can be correlated with the material orientation (its anisotropy). The dimensional information of I_S is used to define the size of an image containing the family of parallel

Fig. 1. Microscale homogenization technique

2.3. Fabric tensor morphologic based method

In order to apply the fabric tensor method, it is necessary to transform the ROI's gray-scale image into a binary image (black and white image), which in this work is identified as I_S. An example of an I_S is shown in the left-upper box of Fig. 1.

The method developed by Whitehouse [19] was used to define the fabric tensor. Thus, the number of interceptions between a parallel family line set, with

lines with $\tau = 0°$. Counting the interceptions of those parallel lines with the boundaries of the binary image square patch, it is possible to obtain the orientation-dependent feature. The ODF of the I_S can be obtained by rotating the family of parallel line image with τ between 0° and 180°, and then counting the interception of the family of parallel lines with the square patch binary image I_S. The created data for τ between [180°, 360°] is a [0°, 180°] data repetition, because the orientation-dependent feature is not influenced by the direction (it only depends on the orientation).

In order to obtain the material orientation, the ODF data was plotted using polar coordinates. This data was then fitted into an ellipse. Observing now both central boxes of Fig. 1, it is perceptible that it is possible to obtain the material orientation of the trabecular micropatch from the ellipse orientation. In addition, from the fitted ellipse, it is possible to obtain the ellipse minor axis length, β_{min}, and major axis length, β_{max}, and θ, the angle of ellipse major axis with the polar plot horizontal axis.

2.4. Phenomenological material law method

In this work, the homogenized anisotropic mechanical properties of I_S are defined using the information from the fitted ellipse and the average apparent density of the binary image I_S. As shown in Eq. (4), the average apparent density, ρ_{app}, of the binary image I_S can be obtained using the number of white pixels, α_w, and black pixels, α_b, of I_S:

$$\rho_{app} = \left(\frac{\alpha_w}{\alpha_b} \right) \rho_{app}^{cortical}, \tag{4}$$

in which the cortical bone apparent density is considered as $\rho_{app}^{cortical} = 2.1$ g/cm^3. Assuming the phenomenological material law proposed by Belinha and co-workers [3], it is possible to define the axial Young's modulus E_{axial} using the homogenized ρ_{app} from Eq. (4). In order to adjust more closely to the experimental results, Belinha's phenomenological law is divided in two equations [3]. Thus, if $\rho_{app} \leq$ 1.3 Eq. (5) should be applied, otherwise Eq. (6) should be used. The coefficients a_j and b_j can be found in Table 1.

$$E_{axial} = \sum_{j=0}^{3} a_j \rho_{app} \quad if \quad \rho_{app} \leq 1.3 \tag{5}$$

$$E_{axial} = \sum_{j=0}^{3} b_j \rho_{app} \quad if \quad \rho_{app} > 1.3 \tag{6}$$

Table 1. Coefficients from Belinha's material law [3]

	$j = 0$	$j = 1$	$j = 2$	$j = 3$
a_j	$0.0E + 00$	$7.216E + 02$	$8.059E + 02$	$0.0E = 00$
b_j	$-1.770E + 05$	$3.861E + 05$	$-2.798E + 05$	$6.836E + 04$

The transverse elastic modulus E_{transv} is defined using the relation between the ellipse minor axis length, β_{min}, and major axis length, β_{max}, as shown in Eq. (7),

$$E_{transv} = \frac{(\| \beta_{min} \| E_{axial})}{\| \beta_{max} \|}. \tag{7}$$

Considering the well-known mixture theory, it is possible to define the Poisson's coefficient, v, using the relation between white and black pixels. Notice that white pixels represent solid bone (for which it was assumed $v = 0.3$) and black pixels represent void space (for which it was assumed $v = 0.0$).

$$v = \frac{0.0(\alpha_b) + 0.3(\alpha_w)}{\alpha_t}. \tag{8}$$

In Eq. (8), α_t represents the total number of pixels of the binary image I_S. The shear modulus, G, was expeditiously calculated using Eq. (9).

$$G = \frac{E_{axial}}{2(1 + v)}. \tag{9}$$

After defining all the required homogenized material properties (E_{axial}, E_{transv}, v and G), it is possible to build the constitutive matrix: $c_{ox'y'}$, for the $ox'y'$ local coordinate system (oriented with the material principal axis, following the principal directions 'axial' and 'transverse'). In fact, defined the orthotropic compliance matrix for the material axis $ox'y'$ is defined. Only after, $c_{ox'y'}$ is defined with $c = s^{-1}$ for this it is necessary to rotate the $c_{ox'y'}$ to the global axis using the angle θ obtained from the ellipse fitting, using the transformation rotation matrix T, Eq. (10),

$$T(\theta) = \begin{bmatrix} \cos(\theta) & -\sin(\theta) & 0 \\ \sin(\theta) & \cos(\theta) & 0 \\ 0 & 0 & 1 \end{bmatrix} \tag{10}$$

and then, finally, it is possible to write the material constitutive matrix in the global axis with Eq. (11),

$$c_{oxy} = T(\theta)^T c_{ox'y'} T(\theta) = \begin{bmatrix} c_{11} & c_{12} & c_{13} \\ c_{21} & c_{22} & c_{23} \\ c_{31} & c_{32} & c_{33} \end{bmatrix} \tag{11}$$

3. Results

Aiming to validate the proposed homogenization methodology, some numerical tests were performed. The tests involved size and rotation analyses of predefined I_S binary images and static analysis using the homogenized material properties.

First, a study in which the RVE size is varied was presented, allowing to understand the influence of this scale parameter in the accuracy of the proposed methodology. Second, in order to access the robustness of the proposed technique, a predefined binary image showing a clear preferential material orientation was analyzed. Afterwards, the input image was rotated, and it was verified if the ellipse fitted from the fabric tensor based methodology had $\beta_{\max}$ aligned with the material orientation of the image. In this validation example, angle increments of 20° were assumed for the family of parallel lines rotation.

In the end, in order to show the efficiency and accuracy of the proposed homogenization technique, a numerical structural analysis using two distinct geometrical models (a homogeneous model and a heterogeneous model) was performed. To show the versatility of the proposed methodology, the technique was combined with two distinct numerical methods, the FEM and the RPIM. For the FEM formulation, in this study, the standard plane strain triangular element was used. Concerning the RPIM formulation used in this work, influence-domain with 16 nodes inside was assumed; one integration point per each integration triangular cell (matching the triangular elements of the FEM analysis for comparison proposes); the MQ-RBF shape parameters suggested in the literature ($c = 0.0001$ and $p = 0.9999$); and a constant polynomial basis.

3.1. Validation of MIL methodology

3.1.1. RVE size

In this section, two distinct RVE models were constructed, Fig. 2a and 2d. The RVE model shown in Fig. 2a is a benchmark fabricated unitary binary image possessing a well-defined material orientation (90°). In order to understand the influence of size of the RVE in the proposed methodology, this fabricated model was repeated $r_n \times r_n$, r_n being the number of repetitions of the RVE. For illustration purposes, Fig. 2b shows its 2×2 repetition and in Fig. 2c its 10×10 repetition is shown. Regarding the model of Fig. 2d, it represents a realistic trabecular square patch unitary binary image obtained from a micro-CT image. Likewise, this realistic RVE was repeated $r_n \times r_n$. In Fig. 2e and 2f examples for the 2×2 repetition and 10×10 repetition, respectively, are shown.

The homogenization methodology proposed was applied to all models: fabricated image and realistic image, and corresponding RVE repetitions ($r_n = 1, 2, 3, ..., 10$). Thus, all the components of the constitutive tensor c_{axy}, Eq. (11) , were obtained for each one of the analyzed RVEs. Thus, Figures 3a and 3b show the components of the constitutive matrix that are obtained using the proposed homogenization methodology for the fabricated benchmark RVE and the realistic trabecular RVE, respectively.

As Eq. (11) and Fig. 1 indicate, angle θ represents the approximated orientation of the material. Thus, using the developed methodology, the angle θ for each RVE model (and corresponding repetitions) was obtained and the results are presented in Table 2. For the fabricated benchmark RVE, an average value of 90°

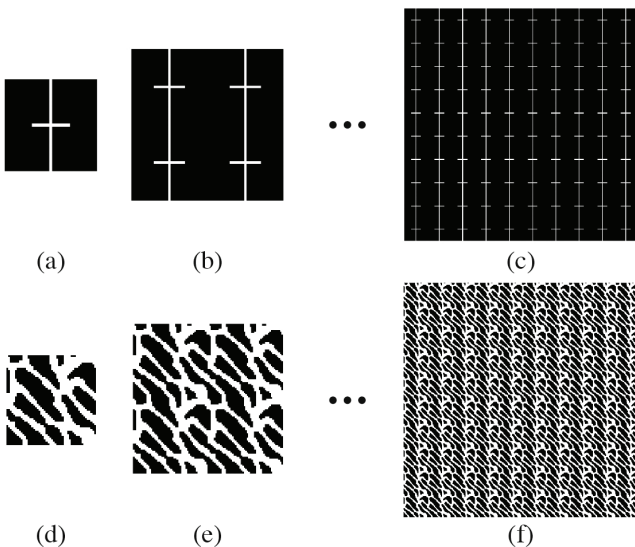

(a)   (b)   ...   (c)

(d)   (e)   ...   (f)

Fig. 2. Binary images used to verify the MIL dependence on the RVE size: Benchmark fabricated unitary image (a), realistic binary image from a micro-CT (d); To analyze the effect of using different RVE sizes, the binary images were repeated from a 2×2 repetition, (b) and (e) to a 10×10 repetitions (c) and (f), respectively

(a)

■ Difference Between Obtained and Expected in Trabecular   ■ Difference Between Obtained and Expected in Created

(b)

■ Obtained in Trabecular Figure   ■ Expected in Trabecular Figure   ■ Obtained in Created Figure   ■ Expected in Created Figure
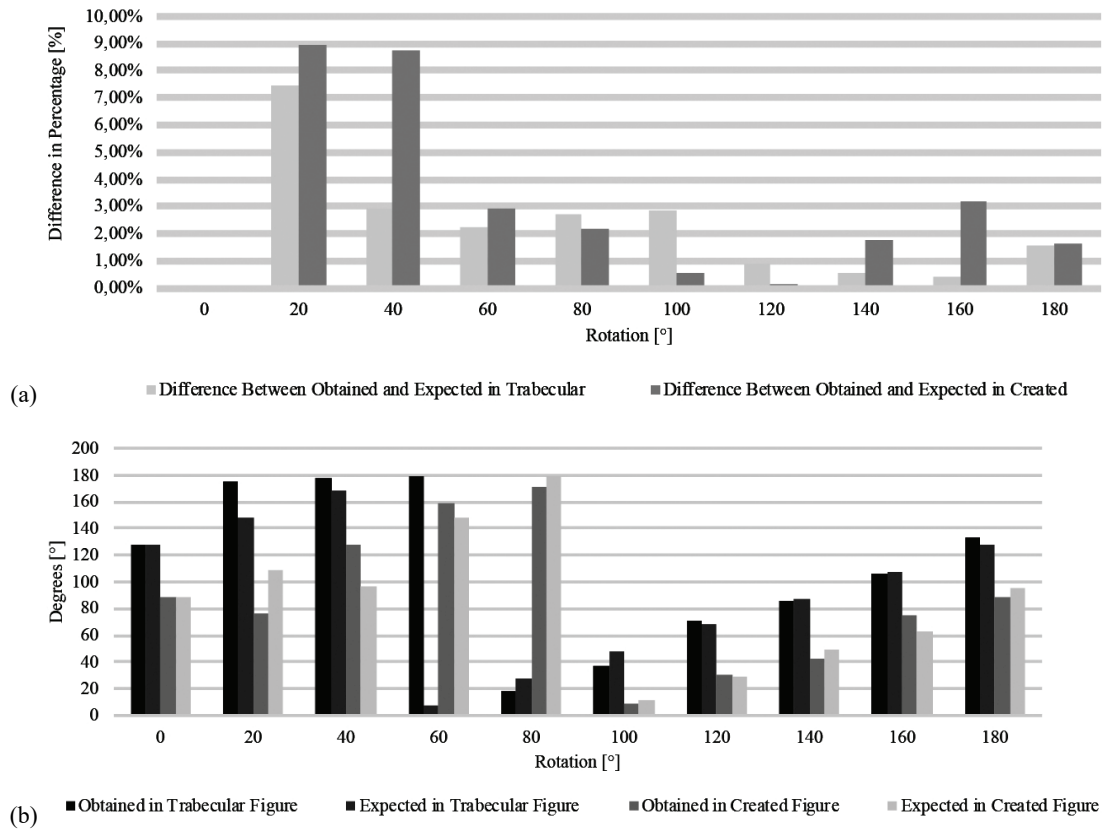
Fig. 3. Constitutive matrix values obtained using a image up to 10× repetitions:
(a) results for realistic, (b) results for the benchmark image

Table 2. Relation between the image repetition and θ

	Repetition	1	2	3	4	5	6	7	8	9	10	Average	SD
θ	Created	90	90	90	90	90	90	90	90	90	90	90	0
	Trabecular	124	127	126	127	127	127	127	127	127	127	127	0

with a standard deviation of 0° was obtained. For realistic trabecular RVE, an average value of 127° with a standard deviation of 0° was obtained.

3.1.2. RVE Rotation

In order to verify whether the developed method is capable to deliver accurate material orientations, an RVE rotation study was performed. The two created models, the benchmark fabricated RVE, Fig. 2a, and the realistic trabecular RVE, Fig. 2d, were rotated in relation the their initial position following increment angles of 20°, between the interval [0°, 180°]. As Figs. 4 and 5 show, it is possible to visualize the orientation/size of the produced ellipse and the corresponding approximated material angle.

3.2. Stress analysis

In this section, distinct RVEs were structurally analyzed using two distinct discretization techniques, the FEM and the RPIM. This study aimed to verify if a homogeneous RVE is capable to produce a homogenized von Mises effective stress similar to the one obtained with a heterogeneous RVE. The homogenized orthotropic mechanical properties were obtained with proposed method.

Therefore, the realistic trabecular RVE previously presented, Fig. 2d, and its $r_n \times r_n$ repetitions were structurally analyzed using the elasto-static formulation. The obtained results were compared with the ones obtained with a homogeneous RVE using much lower discretization levels.
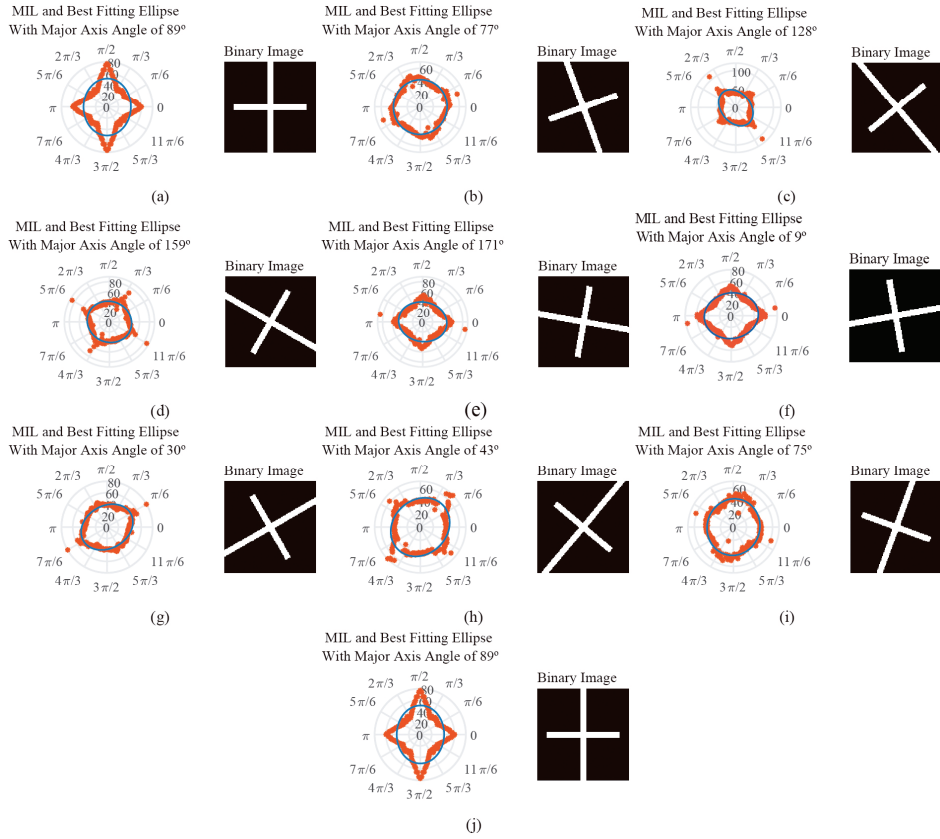
Fig. 4. Benchmark fabricated RVE rotation results: (a) 0° rotation, (b) 20° rotation, (c) 40° rotation, (d) 60° rotation, (e) 80° rotation, (f) 100° rotation, (g) 120° rotation, (h) 140° rotation, (i) 160° rotation, (j) 180° rotation
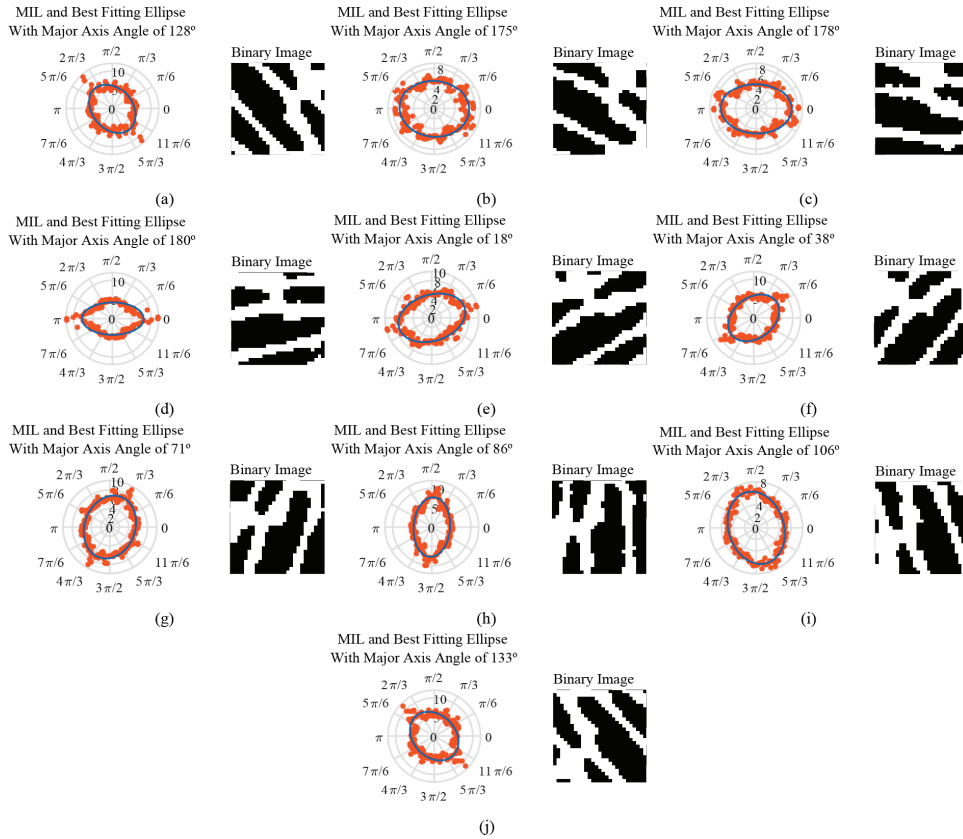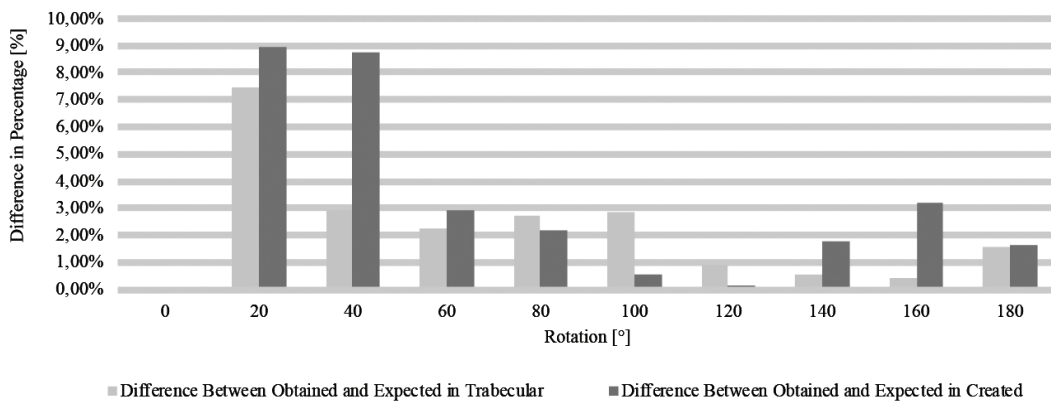

Fig. 5. Realistic trabecular RVE rotation results: (a) 0° rotation, (b) 20° rotation, (c) 40° rotation, (d) 60° rotation, (e) 80° rotation, (f) 100° rotation, (g) 120° rotation, (h) 140° rotation, (i) 160° rotation, (j) 180° rotation

Fig. 6. (a) obtained material orientation angles θ of the fitted ellipse
versus the expected ones for the benchmark fabricated RVE (Fig. 2a) and the realistic trabecular RVE (Fig. 2b),
(b) Difference between the obtained θ results and the expected ones, in percentage

All the analyzed RVEs were squares micro patches with dimensions $L \times L$ and were submitted to the same essential boundary conditions, Fig. 7. Thus, a displacement of $0.1 \times L$ at the nodes of the top layer was imposed, $y = L$. The nodes at $x = 0$ and $x = L$ where constrained along Ox direction, $\bar{u} = 0$, and the nodes at $y = 0$ and $y = L$ were constrained along Oy direction, $\bar{v} = 0$.
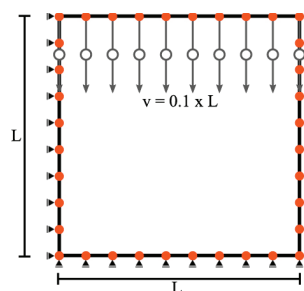
As shown in Fig. 8a, the homogeneous RVE is typically discretized by a set of $n \times n$ nodes uniformly distributed within the RVE domain and every integration point within its domain possess the same homogenized material properties. Conversely, heterogeneous RVEs (realistic trabecular RVE) are formed by trabecular bone and void space. Naturally, as shown in Fig. 8b, the discretization of such complex domain is more demanding. Concerning the element type used in the finite element analyses, in the case of the heterogeneous model, it were used plane strain/plane stress 2D triangular elements with 3 nodes. Alternatively, for the homogeneous model, the authors have considered 2D Lagrangian quadrilateral elements with four nodes (full integration scheme).
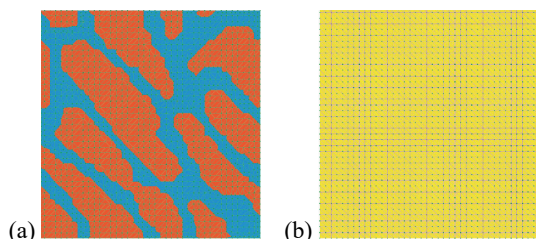
Using the RVE represented in Fig. 2a, and applying the proposed homogenization technique, enabled us to obtain the orthotropic material properties presented in Table 3, column "Homogeneous RVE". Notice that, as already mentioned, every integration point of the homogeneous RVEs will assume these materials properties.

Due to their binary nature, all realistic trabecular RVEs possess or solid bone tissue or void space. Thus, it was necessary to define the material properties of these two domains. Hence, in Table 3 the mechanical properties for the two domains (trabecular bone and void space) were indicated. Following the literature, the mechanical properties of the trabecular bone (solid material) was defined as isotropic [17].

Fig. 7. Boundary conditions applied to all RVEs

Fig. 8. (a) discretized homogeneous RVE
(41×41 nodes uniformly distributed),
(b) example of a discretized heterogeneous RVE
created using micro-CT image information

Table 3. Mechanical properties used in the structural analysis

Mechanical Proprieties							
Homogenized RVE			Trabecular bone		Void Space		
E_{axial}	4488.548	[MPa]	E	11600	[MPa]	E	100	[MPa]
E_{transv}	2520.426	[MPa]						
G	10066.1	[MPa]						
θ	56	[°]						
v	0.3		v	0.36		v	0.459	

Concerning the void domain, the geometrical information coming from the micro-CT forced the existence of a void space between trabeculae. Thus, it was necessary to define the void domain as solid. In order to
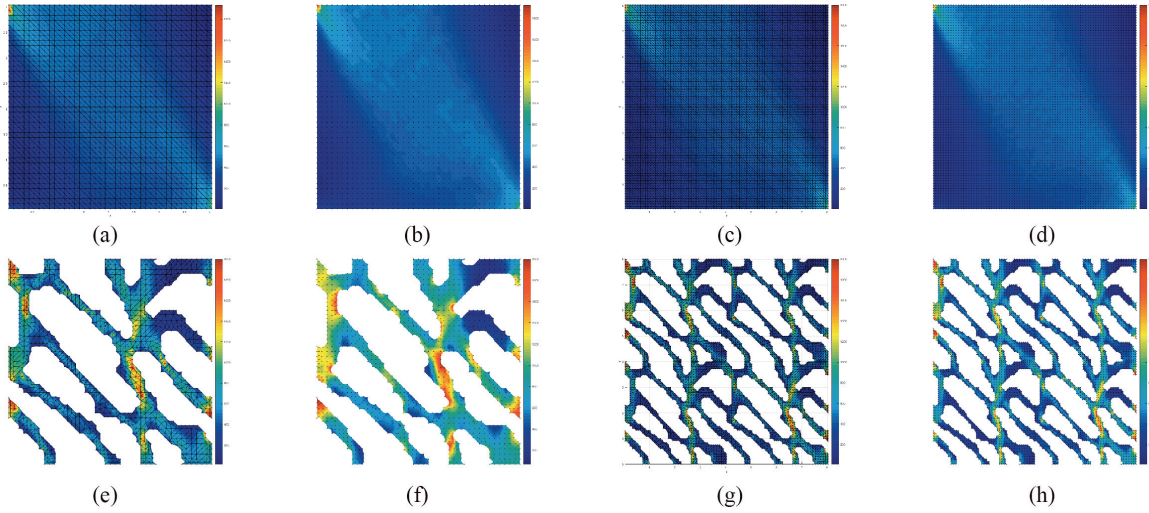
Fig. 9. Effective stress σ_{eff}^h for homogeneous model: (a) FEM 1 × 1, (b) RPIM 1 × 1, (c) FEM 2×, (d) RPIM 2 × 2, and for heterogeneous models: (e) FEM 1 × 1, (f) RPIM 1 × 1, (g) FEM 2 × 2, (h) RPIM 2 × 2

ensure that the void material does not (significantly) interfere with the global structural response of the RVE, to the "void space" was attributed a Young's modulus with a much lower magnitude, compared to the trabecular bone.

The results from the homogeneous RVEs, regardless the level of the discretization or the used numerical method (FEM or RPIM), were very similar, as can be seen in Figs. 9a and 9b. In these figures the preferential orientation of the material is also perceptible, that was obtained using the developed methodology applied to Fig. 2a. Concerning the heterogeneous RVEs, Fig. 9, the results obtained using FEM are slightly different from the one obtained with the RPIM, as can be seen in Figs. 9e, 9g, 9f and 9h. The von Mises effective stress maps obtained using both FEM and RPIM techniques are presented in Figs. 9a and 9c for the FEM and in Figs. 9b and 9d for the RPIM.

The homogenized stress concept was used to compare the stress fields obtained with the homogeneous RVE and with the heterogeneous RVE. The RVE's von Mises effective stress field (or any other RVE's stress/strain field) can be summarized in one scalar value – the homogenized von Mises effective stress – which can be defined as Eq. (12).

$$\sigma_{eff}^h = \frac{1}{n_Q} \sum_{i=1}^{n_Q} \sigma(\boldsymbol{x}_i)_{eff} \, . \tag{12}$$

The number of integration points discretizing the problem domain not belonging to the boundary of the domain boundary is represented by n_Q. FEM integration mesh is constructed differently from the RPIM. Thus, the integration points of both techniques possess different spatial positions. To minimize this effect in order to avoid the (inaccurate) stress concentrations that appear at the domain boundaries, as shown in Fig. 9 shows, part of the domain was excluded: 2% of the domain boundary integration points that form the complete integration mesh from Eq. (12).
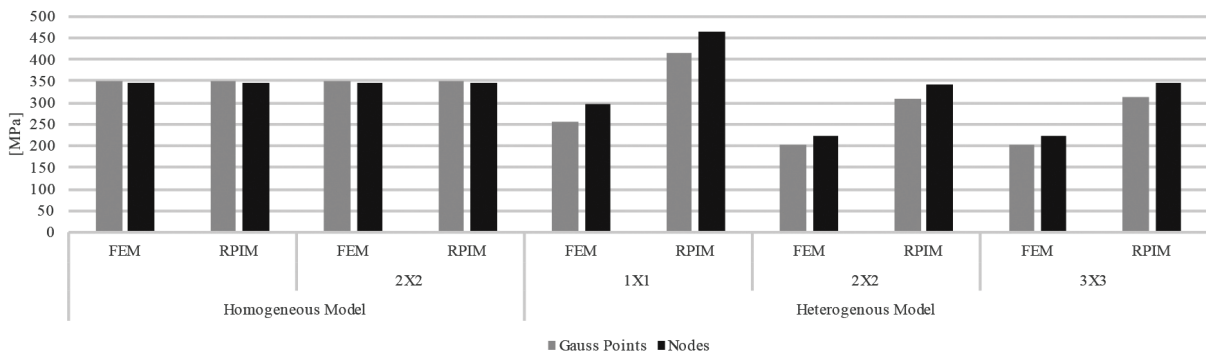

Fig. 10. Homogenized von Mises effective stress σ_{eff}^h obtained with the FEM and the RPIM
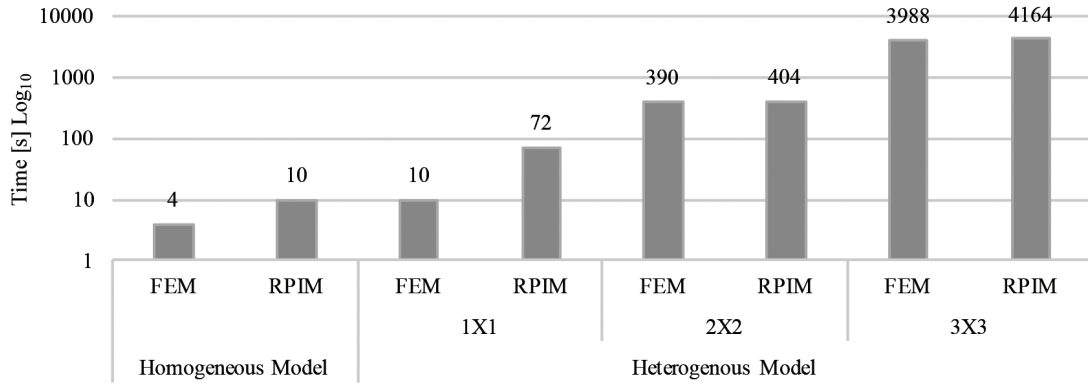
Fig. 11. Computational cost (in seconds) of each analysis

One of the main objectives of this work was to achieve a low-cost and efficient homogenization technique. Thus, in order to understand the computational cost of each analysis, the time-lapse of each structural analysis was recorded. Hence, in Fig. 11 the time-lapse of each structural analysis for the heterogeneous RVEs (with $r_n \times r_n$, $r_n = 1, 2, 3$) and for the homogeneous model (with $r_1 \times r_1$) are shown. In this comparison study, only the computational cost of the 1×1 homogeneous model is presented, since, as can be seen in Fig. 10, it provides a similar result when compared with the 2×2, and it also provides a close result when compared with the 3×3 heterogeneous model.

4. Discussion

Regarding the RVE size analysis, it is possible to visualize in both figures the evolution of c_{ij} with respect to the number of repetitions of the corresponding basic unit RVE. Notice that for both RVEs types (benchmark and realistic), the value of each component of the constitutive matrix, c_{ij}, does not vary significantly with the number of repetitions, r_n. The results also indicate that for the fabricated benchmark RVE, as expected, θ does not suffer any significant

variation (the average value is 90° with a standard deviation of 0°). For the realistic trabecular RVE the number of repetitions do not relevantly change the material orientation angle of the basic unit RVE, being the obtained average value: 127° with a standard deviation of 0°. Regarding the RVE, rotation some of the differences obtained between the expected orientation and the obtained approximated material orientation θ are related with the modification of the source image due to the rotation process. In Fig. 12 it is perceptible that due to the rotation the initial image is modified. The red circle marks the same region in distinct rotated images, and the modification of that region is visible with the image rotation. This effect is caused by the low number of pixels of the figure. Increasing the number of pixels will lead to lower differences. However, it will lead also to a higher computational cost. The methodology proposed hereby is based on pixel information. Changing of the number of white pixels of the image (a parameter highly related with the calculus of the MIL, as Eq. (3) indicates, result in the modification of the MIL value. This effect can be also observed in Fig. 6, in which the material orientation angles θ of the fitted ellipse and the expected ones are represented.

Regarding the results obtained in Stress Analysis section, the homogenized von Mises effective stresses,
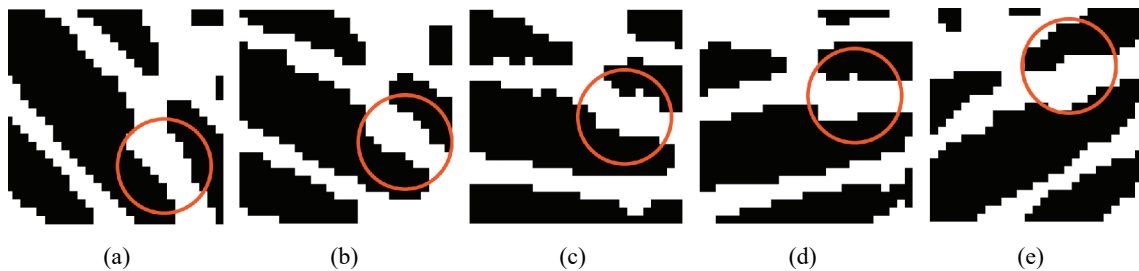

Fig. 12. Image rotation process and inherent morphologic change:
(a) original image, (b) 20° rotation, (c) 40° rotation, (d) 60° rotation, (e) 80° rotation

σ_{eff}^{h}, obtained for each analyzed RVE (using both FEM and RPIM methodologies), are shown in Fig. 10. From this figure it is perceptible that for the considered heterogeneous RVEs, as the model detail increases, σ_{eff}^{h} decreases. Notice that the model detail is governed by the number of repetitions (the 1×1 RVE has a lower detail than the 3×3 RVE). The analyses of the homogeneous models, regardless the discretization technique (FEM or RPIM) or the repetition pattern (1×1 and 2×2), present very similar results. Furthermore, these results are also very similar with the ones obtained with the RPIM using the 2×2 and 3×3 repetition heterogeneous models. Such similarity indicates that the proposed homogenization technique is capable to approximate the homogenized orthotropic material properties of a trabecular patch. Comparing the FEM with the RPIM, it is visible that the results obtained with the homogeneous RVEs are equivalent. However, the FEM and RPIM results obtained with the heterogeneous RVEs are not so close. This difference could be explained by locking effects in the FEM (plane strain triangular elements are being used).

Concerning the computational cost presented in Fig. 10, it was shown that the 3×3 heterogeneous RVE produces results very close with the 1×1 homogeneous RVE. However, Figure 11 shows that the 3×3 heterogeneous RVE takes 4164 s to analyze and the homogeneous RVE only requires 4–10 s. Commonly, multiscale techniques use highly discretized RVEs, leading to high computational costs. However, as this study demonstrates, the proposed homogenization methodology is capable to reduce significantly the cost of a multiscale analysis, enabling more demanding and complex simulations.

5. Conclusions

In this work, a new multiscale method was proposed. The method uses a homogenization technique that, without any a priori knowledge, enables us to estimate the material properties of bone tissue using standard imaging techniques. The results obtained show that the methodologies used to create the fabric tensor and to obtain the mechanical properties are stable. Regarding the RVE size studies, it was demonstrated that the methodology is capable to consistently approximate the bone tissue material mechanical properties. It is expected that the proposed technique will be capable to reduce the cost of the multiscale

analyses, allowing to simulate more complex problems.

References

[1] Abdelwahed B., Abdessalem C., Tarek M., Ridha H., Ali M., *Multiscale approach including microfibril scale to assess elastic constants of cortical bone based on neural network computation and homogenization method*, International Journal for Numerical Methods in Biomedical Engineering, 30 (3), 318–338, DOI: 10.1002/cnm.2604.

[2] Belinha J., *Meshless Methods in Biomechanics: Bone Tissue Remodelling Analysis*, V.E. Brimkov, R.P. Barneva (Eds.), Dordrecht: Springer Netherlands; 2014. (Lecture Notes in Computational Vision and Biomechanics), DOI: 10.1007/978-94-007-4174-4.

[3] Belinha J., Jorge R.M.N., Dinis L.M.J.S., *A meshless microscale bone tissue trabecular remodelling analysis considering a new anisotropic bone tissue material law*, Computer Methods in Biomechanics and Biomedical Engineering. 2012, 5842 (August 2012), 1–15, DOI: 10.1080/10255842.2012.654783.

[4] Belytschko T., Lu Y.Y., Gu L., *Element-free Galerkin methods*, International Journal for Numerical Methods in Engineering, 1994, 37 (2), 229–256, http://onlinelibrary.wiley.com/doi/10.1002/nme.1620370205/abstract [accessed: May 9, 2016], DOI: 10.1002/nme.1620370205.

[5] Carter D.R., Fyhrie D.P., Whalen R.T., *Trabecular bone density and loading history: Regulation of connective tissue biology by mechanical energy*, Journal of Biomechanics, 1987, 20 (8), 785–794, DOI: 10.1016/0021-9290(87)90058-3.

[6] Carter D.R., Van Der Meulen M.C., Beaupré G.S., *Mechanical factors in bone growth and development*, Bone, 1996, 18 (1 Suppl.), 5S–10S, DOI: 10.1016/8756-3282(95)00373-8.

[7] Cowin S.C., *The relationship between the elasticity tensor and the fabric tensor*, Mechanics of Materials, 1985, 4 (2), 137–147, DOI: 10.1016/0167-6636(85)90012-2.

[8] Cowin S.C., Doty S.B., *Tissue Mechanics*, Springer Science, 2007.

[9] Dinis L.M.J.S., Jorge R.M.N., Belinha J., *A 3D shell-like approach using a natural neighbour meshless method: Isotropic and orthotropic thin structures*, Composite Structures, 2010, 92 (5), 1132–1142, DOI: 10.1016/j.compstruct.2009.10.014.

[10] Dorozhkin S.V., *Nanosized and nanocrystalline calcium orthophosphates*, Acta Biomaterialia., 2010, 6 (3), 715–734, DOI: 10.1016/j.actbio.2009.10.031.

[11] Hart R.T., Davy D.T., Heiple K.G., *A Computational Method for Stress Analysis of Adaptive Elastic Materials With a View Toward Applications in Strain-Induced Bone Remodeling*, Journal of Biomechanical Engineering, 1984, 106 (4), 342, DOI: 10.1115/1.3138503.

[12] Huiskes R., Chao E.Y.S., *A survey of finite element analysis in orthopedic biomechanics: The first decade*, Journal of Biomechanics, 1983, 16 (6), 385–409, DOI: 10.1016/0021-9290(83)90072-6.

[13] Landis W.J., *The strength of a calcified tissue depends in part on the molecular structure and organization of its constituent mineral crystals in their organic matrix*, Bone, 1995, 16 (5), 533–544, DOI: 10.1016/8756-3282(95)00076-P.

[14] Liu W.K., Jun S., Zhang Y.F., *Reproducing kernel particle methods*, International Journal for Numerical Methods in Fluids, 1995, 20 (8–9), 1081–1106, DOI: 10.1002/fld.1650200824.

[15] Moreno R., Borga M., Smedby O., *Techniques for Computing Fabric Tensors – A Review*, [in:] *Mathematics and Visualization*, 2014, Vol. 5. 271–292, DOI: 10.1007/978-3-642-54301-2_12.

[16] Moreno R., Smedby Ö., Pahr D.H., *Prediction of apparent trabecular bone stiffness through fourth-order fabric tensors*, Biomechanics and Modeling in Mechanobiology, 2016, 15 (4), 831–844, http://link.springer.com/10.1007/s10237-015-0726-5, [accessed: Nov. 14, 2016], DOI: 10.1007/s10237-015-0726-5.

[17] Natali A.N., Carniel E.L., Pavan P.G., *Constitutive modelling of inelastic behaviour of cortical bone*, Medical Engineering and Physics, 2008, 30 (7), 905–912, DOI: 10.1016/j.medengphy.2007.12.001.

[18] Wang J.G., Liu G.R., *A point interpolation meshless method based on radial basis functions*, International Journal for Numerical Methods in Engineering, 2002, 54 (11), 1623–1648, http://doi.wiley.com/10.1002/nme.489 [accessed: May 9, 2016], DOI: 10.1002/nme.489.

[19] Whitehouse W.J., *The quantitative morphology of anisotropic trabecular bone*, Journal of Microscopy, 1974, 101 (2), 153–168, DOI: 10.1111/j.1365-2818.1974.tb03878.x.

[20] Wnek G.E., Bowlin G.L., *Encyclopedia of Biomaterials and Biomedical Engineering*, 2nd Ed., G.E. Wnek, L.B. Gary (Eds.), CRC Press, New York 2008.

[21] Wolff J., *The Law of Bone Remodelling*, Journal of Anatomy, 1886, 155, 217, DOI: 10.1097/00006534-198810000-00036.

[22] Zysset P.K., *A review of morphology–elasticity relationships in human trabecular bone: theories and experiments*, Journal of Biomechanics, 2003, 36(10), 1469–1485, https://www.sciencedirect.com/science/article/pii/S0021929003001283, [accessed: Apr. 16, 2018] DOI: 10.1016/S0021-9290(03)00128-3.